Research in Astronomy and Astrophysics, 24:125020 (10pp), 2024 December https://doi.org/10.1088/1674-4527/ad8b0d

A Real-time Monitor for TeV Gamma-Ray Flare with the LHAASO-WCDA Detector

G. M. Xiang[1,2], M. Zha[3], J. N. Zhou[1], and Y. Xing[1]
[1] Key Laboratory for Research in Galaxies and Cosmology, Shanghai Astronomical Observatory, Chinese Academy of Sciences, Shanghai 200030, China; gmxiang@shao.ac.cn
[2] University of Chinese Academy of Sciences, Beijing 100049, China
[3] Key Laboratory of Particle Astrophysics, Institute of High Energy Physics, Chinese Academy of Sciences, Beijing 100049, China
Received 2024 April 11; revised 2024 September 26; accepted 2024 October 17; published 2024 December 13

Abstract

With its high duty cycle, wide field of view and high detection sensitivity, Water Chereknov Detector Array as one of sub-arrays of Large High Altitude Air Shower Observatory is a promising facility to monitor transient phenomena in the very high energy gamma-ray band. In this work, a real-time monitor for selected TeV extragalactic sources is introduced, this flare monitor is developed to detect very high energy flare events and for further studying the power-providing mechanism of blazar relativistic jets. The detailed information such as the searching method and sensitivity of this real-time flare monitor is also presented. In the end, successful multi-wavelength and multi-messenger observation of 1ES 1959+650 and IC 310 also confirms the capabilities and reliability of the monitoring system.

Key words: methods: data analysis – methods: observational – gamma-rays: galaxies

1. Introduction

Blazars are one of the most powerful objects in the Universe and comprise the majority of gamma-ray sources in the extragalactic sky. Observations of blazars and their variability have been an active field of research. Based on long-term observations, blazars have shown the variability over different timescales ranging from minutes to days, months and even longer. Due to their favorable jet orientation, blazars have some of the most observable energetic phenomena and extremely high gamma-ray luminosities, many multi-wavelength campaigns have been deployed, providing many important information on source acceleration models and the inner engine or black hole. For example the study of Very High Energy (VHE) flares from blazars can provide insights into the VHE emission mechanism during flares and help distinguish between the two emission scenarios, such as Synchrotron Self-Compton (SSC) model (Stecker et al. 1992), and photon-hadronic model (Ghisellini et al. 1998). Furthermore, observations of VHE flare events can be tools to study other physics topics such as the extragalactic background light (Dwek & Krennrich 2013), intergalactic magnetic field (Neronov & Semikoz 2007), and Lorentz invariance violation (Biller et al. 1999).

While a lot of research has been conducted on extragalactic VHE flares by various feasilities, such as the gamma-ray sky survey (Abdollahi et al. 2017; Ajello et al. 2017) by Fermi-LAT covering the 30 MeV–300 GeV energy range (Ajello et al. 2021), the limitations of the detector's effective area in the VHE band have resulted in insufficient statistics to detect VHE transients. Furthermore, ground-based Imaging Atmospheric Cherenkov Telescopes (IACTs) has been limited by their pointing nature and small field of view (FOV). Simultaneously, ground-based extensive air shower arrays have also carried out a series of studies on VHE transients, such as an early warning monitor implemented on ARGO-YBJ experiment (Bartoli et al. 2011). Despite being a large FOV detector, due to its limited sensitivity, only three flares of Mkn 421 during operation has been reported.

With unprecedented detection sensitivity, (around 1.5% Crab Unit) and large FOV (around 2 Steradians) and high duty cycle (higher than 98%) LHAASO-WCDA has the capability to continually and unbiased survey the sky of the northern hemisphere at VHE band. These features make WCDA an ideal instrument to conduct real-time analysis of the extragalactic transients events and provide new opportunities for the discovery of extragalactic blazar flares. Once a flare is identified by the WCDA, an alert could be sent to other multi-wavelength instruments, such as Fermi-LAT, Swift, IACTs, and multi-messenger facility such as ICECUBE, to trigger follow-up observations on a global scale.

Here we report the development and deployment of a real-time flare monitor designed to monitor VHE flare using the LHAASO-WCDA. After a brief introduction of the LHAASO-WCDA in Section 2, we outline the mechanics of the flare monitor and discuss the setting for false alarm rates in Section 3, the candidate sources are also included in Section 3. The flare monitor sensitivity is presented in Section 4. Subsequently, we present the results from test running data in Section 5. Finally,

we provide a summary and outlook of this real-time monitoring system.

2. The LHAASO-WCDA Detector

The Large High Altitude Air Shower Observatory (LHAASO) is located at Haizi mountain, Daochen (4410 m a.s.l., 606 g cm^{-2}, 29°21′31″ N, 100°08′15″ E) Sichuan Province, China. Water Cherenkov Detector Array (WCDA) consists of three separate pools with a total area of 78,000 m^2. The area of No.1 pool and No.2 is 150 × 150 m^2 with 900 detection units with the size of 5 × 5 m^2, and the area of the 3rd pool (No.3) is 300 × 110 m^2 with 1320 detection units. Each detection unit is separated by black plastic curtains to block the scattered light from other units. Each detection unit is equipped with a big photomultiplier(PMT) and a small PMT to enlarge the dynamic range. The No.1 pool is installed with 8-inch PMT and 3-inch PMT of each detection unit. In order to lower threshold energy, the detection units of No.2 and No.3 pools are installed with 20-inch PMT and 3-inch PMT.

By sampling the energy deposition and arrival time in each detection unit caused by the air shower secondary particles, the direction and the energy information related with primary particles can be reconstructed. In order to pick up gamma-like events, a composition sensitive parameter, noted as Pincness, with cut value of less than 1.1, is required to pick up gamma-like air shower events, additionally only events with zenith angle less than 45° are utilized for later monitoring analysis to ensure the quality of reconstruction data. More details about the detector and the reconstruction algorithm can be found in (Aharonian et al. 2021; Cao et al. 2024).

3. Flare Monitor Scheme

The whole monitor scheme is composed of four main elements, we will describe them one by one in the following text.

1. target sources selection
2. background estimation method
3. search for excess
4. flare monitor trigger condition.

3.1. Target Source Selection

Target sources were selected on the knowledge or perceived probability of VHE gamma-ray emission from the source. A list of potential VHE extragalactic candidates was chosen from an online catalog for TeV Astronomy (TeVCat; Wakely & Horan 2008) and the Third Catalog of Hard Fermi-LAT Sources (3FHL; Ajello et al. 2017). TeVCat includes 251 detected VHE sources, including both galactic and extragalactic sources, here only 66 extragalactic sources within the FOV of WCDA are our targets. The 3FHL catalog contains 1556 objects characterized in the 10 GeV–2 TeV energy range. 79% of the detected sources are associated with extragalactic counterparts in multi-wavelength observations and are expected to have the potential to generate VHE gamma-ray radiation, 82 nearby extragalactic sources with redshifts $z < 0.3$ (not included in TeVCat) are included in the target list. The detailed information of all 148 sources can be found in Table 1.

3.2. Background Estimation Method

In order to calculate the excess signal from the source, six events (N_{on}) and background maps (N_{off}) relative to Table 2 are generated by using full sky Hierarchical Equal Area isoLatitude Pixelization (HEALPix) with a resolution of nside of 1024 (Górski et al. 2005). The background maps are computed based on a direct integration method (Fleysher et al. 2004), the detector acceptance is estimated with an integration time of 2 hr. To minimize the impact of certain strong and well-known gamma-ray sources, as well as specific regions, are excluded from the background computation. These regions cover the Crab Nebula, the two Markarians 421, 501, the Geminga region, and a region within ±5° around the inner Galactic Plane. It is important to note that both the event and background maps are smoothed with disk function, taking into account the detector's point-spread function. Here the optimal radius, 1.58 × ρ_{40}, are used, where ρ_{40} is the radius containing 40% of the total events.

In order to ensure the continuous operation of the monitoring system, we utilize the acceptance generated during the same period on the previous day as the acceptance for the specific two-hour duration. A stability test, as mentioned in Fleysher et al. (2004), is conducted on the WCDA test running data to demonstrate feasibility. As shown in Figure 1, the acceptance displays periodic variations, reaching a maximum (less than 3%) at a 12 hr time separation, with the difference between two neighboring days for the same two-hour duration being completely negligible. Therefore, it is reasonable for us to use the acceptance from the previous two-hour period as the acceptance for the current two-hour period.

Due to the low statistics in high N_{nhit} bins, here we are talking about bin 4 and bin 5 in Table 2, a $0.^{\circ}5$ acceptance smoothing radius has been used for low statistics analysis bins implying a large off-source region is employed to estimate the background.

3.3. Search for Excess

The likelihood ratio test is performed to detect flare of the source interested. Here we define the expectation of the number of photons in the on-source region, $\langle N_{on} \rangle$ and the expectation of the number of photons in the off-source region, $\langle N_{off} \rangle$. We assume that the on-source count N_{on} is obtained from a Poisson distribution with mean $\langle N_{on} \rangle$, and the off-source count N_{off} is obtained from a Poisson distribution with mean $\langle N_{off} \rangle$. The

Table 1
Source Candidates for the LHAASO-WCDA Monitor

Name	R.A (°)	Decl. (°)	Flux (Crab Unit)	Index	Redshift
Mkn 421	166.08	38.19	0.3	2.2	0.031
Mkn 501	253.47	39.76	N/A	2.72	0.034
WComae	185.38	28.23	0.09	3.81	0.102
1ES 0033+595	8.82	59.79	0.015	3.8	0.467
S2 0109+22	18.02	22.74	0.03	N/A	N/A
RGB J0136+391	24.13	39.10	N/A	N/A	N/A
RGB J0152+017	28.14	1.78	0.02	2.95	0.08
TXS 0210+515	33.57	51.75	N/A	1.9	0.049
S3 0218+35	35.27	35.94	0.3	3.8	0.954
3C 66A	35.67	43.04	0.06	4.1	0.34
MAGIC J0223+403	35.80	43.01	0.022	3.1	N/A
1ES 0229+200	38.22	20.27	0.018	2.5	0.1396
IC 310	49.18	41.32	0.025	N/A	0.0189
RBS 0413	49.95	18.76	0.01	N/A	0.19
NGC 1275	49.95	41.51	0.025	4.1	0.017559
1ES 0347-121	57.35	−11.98	0.02	3.1	0.188
1ES 0414+009	64.22	1.09	0.006	3.45	0.287
1ES 0502+675	76.98	67.62	0.06	N/A	0.34
TXS 0506+056	77.35	5.70	0.016	4.8	0.3365
VER J0521+211	80.44	21.21	0.092	3.44	N/A
RX J0648.7+1516	102.19	15.27	0.033	4.4	0.179
1ES 0647+250	102.69	25.05	0.03	N/A	N/A
RGB J0710+591	107.61	59.15	0.03	2.69	0.125
S5 0716+714	110.47	71.34	N/A	3.45	N/A
PKS 0736+017	114.82	1.60	0.1	3.1	0.18941
1ES 0806+524	122.50	52.32	0.018	2.65	0.138
RBS 0723	131.80	11.56	0.025	N/A	0.198
OJ 287	133.70	20.10	0.013	3.49	0.3056
M82	148.97	69.68	0.009	2.5	3900 kpc
S4 0954+65	149.70	65.57	N/A	N/A	0.3694
1ES 1011+496	153.77	49.43	0.05	3.66	0.212
Markarian 180	174.11	70.16	0.11	N/A	0.045
RX J1136.5+6737	174.12	67.62	0.015	N/A	0.1342
3C 264	176.27	19.61	0.01	N/A	0.021718
TON 0599	179.88	29.25	0.3	N/A	0.7247
1ES 1215+303	184.45	30.10	0.035	N/A	0.131
1ES 1218+304	185.36	30.19	0.08	N/A	0.182
MS 1221.8+2452	186.10	24.61	0.04	N/A	0.218
4C+21.35	186.22	21.38	0.03	3.75	0.432
S3 1227+25	187.56	25.30	0.07	N/A	0.325
M 87	187.70	12.40	0.075	N/A	0.0044
3C 279	194.05	−5.79	N/A	4.1	0.5362
B2 1420+32	215.62	32.39	0.15	3.57	0.682
PKS 1424+240	216.75	23.79	0.05	4.2	N/A
H 1426+428	217.13	42.67	0.03	3.5	0.129
1ES 1440+122	220.81	12.00	0.01	3.1	0.163
PKS 1441+25	220.98	25.03	0.16	N/A	0.939
PKS 1510-089	228.22	−9.11	0.03	3.26	0.361
PG 1553+113	238.93	11.19	0.034	4.5	N/A
H 1722+119	261.27	11.87	0.02	N/A	N/A
1ES 1727+502	262.07	50.22	0.021	N/A	0.055
1ES 1741+196	266.00	19.55	0.016	2.7	0.084
OT 081	267.88	9.65	0.08	N/A	0.322
B2 1811+31	273.40	31.74	0.05	N/A	0.117
1ES 1959+650	300.00	65.15	0.64	N/A	0.048
MAGIC J2001+435	300.31	43.88	0.09	2.8	0.1739

Table 1
(Continued)

Name	R.A (°)	Decl. (°)	Flux (Crab Unit)	Index	Redshift
1ES 2037+521	309.85	52.33	0.03	N/A	0.053
RGB J2056+496	314.17	49.67	0.029	N/A	N/A
BL Lacertae	330.68	42.28	0.03	3.6	0.069
RGB J2243+203	340.97	20.32	0.14	4.6	N/A
B3 2247+381	342.52	38.43	0.04	3.2	0.1187
1ES 2344+514	356.77	51.71	0.07	2.46	0.044
1RXS J081201.8+023735	123.00	2.63	N/A	N/A	0.1721
GB6 J1058+2817	164.62	28.30	N/A	N/A	N/A
NGC 1068	40.66	0.01	N/A	N/A	14Mpc
PGC 2402248	113.36	51.90	0.01	2.41	0.065
3FHL J0007.9+4711	1.993	47.192	0.017	2.859	0.280
3FHL J0018.6+2946	4.653	29.782	0.006	1.982	0.100
3FHL J0037.8+1239	9.462	12.651	0.006	2.530	0.089
3FHL J0047.9+3947	11.977	39.790	0.010	2.333	0.252
3FHL J0059.3-0152	14.839	−1.875	0.005	2.219	0.144
3FHL J0159.5+1047	29.882	10.788	0.010	2.669	0.195
3FHL J0216.4+2315	34.113	23.254	0.004	2.286	0.288
3FHL J0217.1+0836	34.276	8.605	0.008	2.983	0.085
3FHL J0242.7-0002	40.676	−0.043	0.004	3.818	0.003
3FHL J0308.4+0408	47.119	4.134	0.006	2.459	0.029
3FHL J0312.8+3614	48.220	36.245	0.004	1.831	0.071
3FHL J0334.3+3920	53.591	39.338	0.004	1.757	0.021
3FHL J0336.4-0348	54.122	−3.800	0.003	1.846	0.159
3FHL J0424.7+0036	66.199	0.603	0.009	2.500	0.268
3FHL J0516.3+7350	79.091	73.850	0.005	2.083	0.251
3FHL J0656.2+4235	104.059	42.596	0.003	1.957	0.059
3FHL J0730.4+3307	112.608	33.120	0.005	2.137	0.112
3FHL J0753.1+5354	118.286	53.907	0.006	2.613	0.200
3FHL J0814.6+6429	123.653	64.491	0.010	2.453	0.239
3FHL J0816.9+2050	124.236	20.847	0.004	2.311	0.058
3FHL J0828.3+4153	127.088	41.898	0.002	1.980	0.226
3FHL J0831.8+0429	127.961	4.496	0.012	3.636	0.174
3FHL J0850.6+3454	132.652	34.907	0.004	2.256	0.145
3FHL J0908.9+2311	137.238	23.191	0.013	2.499	0.223
3FHL J0912.4+1555	138.124	15.930	0.003	1.843	0.212
3FHL J0930.4+4952	142.624	49.875	0.004	1.972	0.187
3FHL J0932.1+6736	143.041	67.614	0.002	3.152	0.023
3FHL J0940.5+6149	145.141	61.818	0.003	1.977	0.211
3FHL J0952.3+7502	148.084	75.047	0.004	1.867	0.181
3FHL J1041.7+3900	160.442	39.010	0.002	2.817	0.210
3FHL J1100.3+4020	165.080	40.336	0.008	2.653	0.225
3FHL J1105.8+3944	166.454	39.749	0.003	3.167	0.099
3FHL J1125.9-0743	171.482	−7.720	0.003	2.181	0.279
3FHL J1140.5+1528	175.132	15.480	0.005	2.015	0.244
3FHL J1142.0+1546	175.517	15.777	0.004	2.640	0.299
3FHL J1143.1+6121	175.798	61.353	0.004	2.863	0.049
3FHL J1145.0+1935	176.268	19.590	0.003	1.648	0.022
3FHL J1150.3+2418	177.588	24.301	0.007	3.249	0.200
3FHL J1154.1-0010	178.526	−0.180	0.011	2.494	0.254
3FHL J1203.1+6030	180.781	60.512	0.005	2.052	0.065
3FHL J1208.1+6120	182.043	61.341	0.002	2.807	0.275
3FHL J1219.7-0312	184.927	−3.213	0.007	2.203	0.299
3FHL J1229.2+0201	187.304	2.025	0.006	3.478	0.158
3FHL J1231.4+1422	187.866	14.368	0.006	2.156	0.256
3FHL J1231.6+6415	187.905	64.266	0.005	2.007	0.163
3FHL J1243.0+7316	190.767	73.274	0.002	1.604	0.075
3FHL J1253.7+0328	193.447	3.473	0.006	2.071	0.066

Table 1
(Continued)

Name	R.A (°)	Decl. (°)	Flux (Crab Unit)	Index	Redshift
3FHL J1258.3+6121	194.582	61.367	0.002	3.265	0.224
3FHL J1310.3-1158	197.580	−11.971	0.006	2.204	0.140
3FHL J1341.2+3959	205.313	39.990	0.004	1.953	0.172
3FHL J1402.6+1559	210.654	15.984	0.002	2.362	0.244
3FHL J1411.8+5249	212.965	52.823	0.003	2.146	0.076
3FHL J1419.4+0444	214.868	4.745	0.004	3.338	0.143
3FHL J1419.7+5423	214.947	54.391	0.005	2.265	0.153
3FHL J1449.5+2745	222.385	27.756	0.002	1.959	0.227
3FHL J1500.9+2238	225.248	22.640	0.013	2.338	0.235
3FHL J1508.7+2708	227.188	27.144	0.004	2.043	0.270
3FHL J1512.2+0203	228.072	2.060	0.007	2.804	0.220
3FHL J1518.5+4044	229.645	40.740	0.004	2.655	0.065
3FHL J1531.9+3016	232.986	30.273	0.004	2.365	0.065
3FHL J1543.6+0452	235.900	4.880	0.008	2.296	0.040
3FHL J1554.2+2010	238.571	20.177	0.003	1.678	0.222
3FHL J1603.8+1103	240.951	11.057	0.002	2.400	0.143
3FHL J1615.4+4711	243.867	47.195	0.003	3.073	0.199
3FHL J1643.5-0646	250.891	−6.778	0.004	1.924	0.082
3FHL J1647.6+4950	251.902	49.846	0.006	2.620	0.047
3FHL J1652.7+4024	253.194	40.403	0.004	2.388	0.240
3FHL J1719.2+1745	259.808	17.758	0.016	2.830	0.137
3FHL J1725.4+5851	261.356	58.864	0.003	2.598	0.297
3FHL J1730.8+3715	262.706	37.259	0.004	3.023	0.204
3FHL J1745.6+3950	266.414	39.839	0.002	1.958	0.267
3FHL J1806.8+6950	271.700	69.839	0.015	2.919	0.050
3FHL J1813.5+3144	273.396	31.739	0.006	2.527	0.117
3FHL J2000.4-1327	300.120	−13.451	0.004	2.984	0.222
3FHL J2001.5+7039	300.394	70.665	0.004	2.637	0.254
3FHL J2055.0+0014	313.753	0.236	0.004	2.162	0.151
3FHL J2108.8-0251	317.213	−2.858	0.003	1.803	0.149
3FHL J2143.5+1742	325.899	17.709	0.011	2.666	0.211
3FHL J2145.8+0718	326.453	7.314	0.003	5.503	0.237
3FHL J2252.0+4031	343.022	40.518	0.008	2.263	0.229
3FHL J2338.9+2123	354.745	21.397	0.006	2.252	0.291
3FHL J2356.2+4035	359.075	40.599	0.005	1.910	0.131

Note. N/A stands for no measurement available.

Table 2
Upper and Lower Boundaries of $N_{\rm hit}$ Bins

Bin	$N_{\rm hit}$	ρ_{40} (°)
0	[60–100)	0.67
1	[100–200)	0.43
2	[200–300)	0.29
3	[300–500)	0.23
4	[500–800)	0.18
5	[800–2000)	0.16

Note. ρ_{40} indicates the reconstructed angular resolution for each $N_{\rm hit}$ bin.

likelihood functions for $N_{\rm hit}$ bin i can be expressed as follows:

$$L_i \equiv P(N^i_{\rm on}, N^i_{\rm off}|<N^i_{\rm on}>,<N^i_{\rm off}>) = \frac{e^{-<N^i_{\rm on}>} < N^i_{\rm on}>^{N^i_{\rm on}}}{N^i_{\rm on}!} \frac{e^{-<N^i_{\rm off}>} < N^i_{\rm off}>^{N^i_{\rm off}}}{N^i_{\rm off}!} \quad (1)$$

The null hypothesis that is all detected photons are due to background fluctuation, $L_{b,i}$. $L_{s+b,i}$ is the alter hypothesis of existing flare phenomenon, in other words, all detected photons are from background plus signals. Following the solution described in Li & Ma (1983), the test statistic is defined using

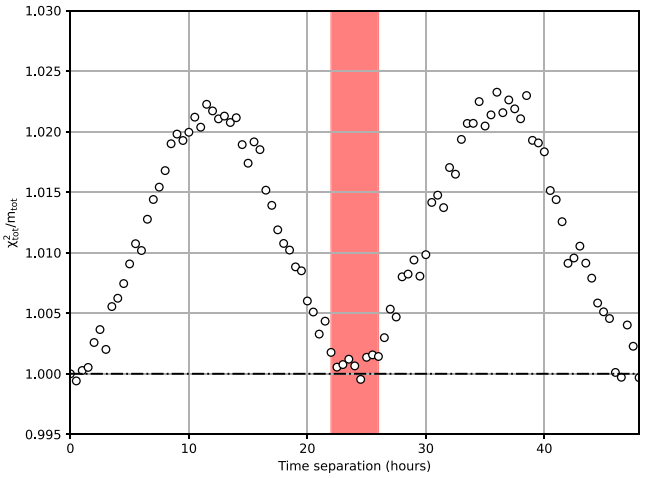

Figure 1. The result of stability test with using WCDA data. The horizontal axis is the time separation from starting time, the vertical axis is the $\chi^2_{\rm tot}(\Delta t)/m_{\rm tot}(\Delta t)$. The black dotted and dashed line is the expected value of 1 if the stability assumption holds. The red area represents the time separation of 24 ± 2 hr.

the likelihood ratio,

$$\begin{aligned} {\rm TS}_i &= 2\ln\frac{L_{s+b,i}}{L_{b,i}} \\ &= 2\ln\{\left[\frac{\alpha^i}{1+\alpha^i}\left(\frac{N^i_{\rm on}+N^i_{\rm off}}{N^i_{\rm on}}\right)\right]^{N^i_{\rm on}} \\ &\times\left[\frac{1}{1+\alpha^i}\left(\frac{N^i_{\rm on}+N^i_{\rm off}}{N^i_{\rm off}}\right)\right]^{N^i_{\rm off}}\} \end{aligned} \quad (2)$$

where α^i is the ratio of the on-source exposure to the off-source exposure for analysis $N_{\rm hit}$ bin i.

The total test statistic is the product of test statistics from $N_{\rm hit}$ bin 0 to $N_{\rm hit}$ bin 6.

$$ {\rm TS}_{\rm tot} = \sum_{i=0}^{k} {\rm TS}_i \quad (3)$$

According to the Wilks' theorem (Wilks 1938), $\rm TS_{tot}$ approximately follows a χ^2 distribution with k degree of freedom.

3.4. Flare Monitor Trigger Condition

When searching for the flares, two factors must be considered: spatial search and time duration search. Because of predefined sky map without the optimization to any sources, in terms of spatial searching, the flare source should not be located exactly in the center of a sky pixel. In order to limit a reasonable angular distance between the sky pixel and the flare source and account for the pointing error of the WCDA detector, the maximum searching radius for the target source is set at $0.^\circ1$. Only the maximum TS value is kept to indicate the significance of the target source.

As for the time duration search, any target source is monitored until it disappeared from the FOV of the detector or reaches its culmination, the test statistic of 0.5, 1, 2, 4 days transits, i.e., $\rm TS_{time}$ are calculated.

Ultimately, the maximum $\rm TS_{tot}$ from all spatial and four time durations is taken to represent the TS value of the target source for that day.

Flare searching specifically focuses on the increase in flux ($N^i_{\rm on} > \alpha^i N^i_{\rm off}$) as the primary concern. When $N^i_{\rm on} < \alpha^i N^i_{\rm on}$ for analysis bin i, Equation (2) will be replaced by 0 for $N_{\rm hit}$ Segment i. Equation (3) takes the form:

$$ {\rm TS}_{\rm tot} = \sum_{i=0}^{k}[0,\ {\rm sign}(N^i_{\rm on} - \alpha^i N^i_{\rm off}){\rm TS}_i] \quad (4)$$

where

$$ {\rm sign}(x) = \begin{cases} 1, & x > 0 \\ 0, & x < 0 \end{cases} \quad (5)$$

In summary, the trigger condition is set as

$$ \max_{\rm (space,time)} {\rm TS}_{\rm tot} > {\rm TS}_{\rm threshold} \quad (6)$$

where $\rm TS_{threshold}$ is the threshold that controls the false alarm rate.

3.4.1. False Alarm Rate

The monitoring system selects maximum TS in space and time duration bins as the TS of the target source for that specific day. However, due to severe correlations between spatial and time duration searches, there is no simple distribution for an excess to calculate the chance probability. In this case, a Monte Carlo simulation of the searching procedure is applied for a single source to sort the TS distribution, assuming that there are no signal emissions from the source. Based on this distribution, the False Alarm Rate (FAR) for a $\rm TS_{threshold}$ can be easily calculated. The work follows three detailed steps in this process.

1. First we determinate the threshold for the source which was located at the same decl. as Crab Nebula (decl. $= 22^\circ$).
2. By simulated sources at other decl. in the FOV of WCDA to check if the threshold is decl.-dependent.
3. for the extragalactic sources with stable strong emission (Mkn 421, Mkn 501), additional corrections to the thresholds has been made to achieve the same false alarm rate for each source.

Totally 10^6 transits simulated samples are produced to calculate the relationship between the false alarm rate and the $\rm TS_{threshold}$ shown in Figure 2. By using interpolation Figure 2 is the distribution between the false alarm rate and threshold parameter. The $\rm TS_{threshold}$ for false alarm rates of 1 flare event

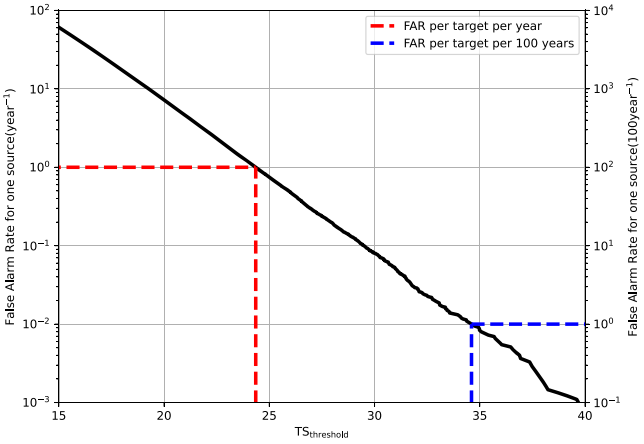

Figure 2. The relationship between False Alarm Rate (FAR) and the $TS_{threshold}$, derived from 10^6 transits of simulated observations at Crab Nebula position.

per target per year and 1 flare event per target per century are $TS_{threshold} = 24.35$ and $TS_{threshold} = 34.60$, respectively.

3.4.2. False Alarm Rate decl. Dependence

Due to the reduced on-source and off-source event counts at large zenith angles, this could potentially have an impact on the threshold. We investigated the relationship between the $TS_{threshold}$ and decl. and introduced a correction for the $TS_{threshold}$. We simulated results from 19 different declinations, ranging from $-10°$ to $+75°$, to determine the dependence of the threshold on decl. and its relationship with the false alarm rate.

The upper panel of Figure 3 shows the $TS_{threshold}$ required for false alarm rates of 1 event per year and 1 event per century. The lower panel of Figure 3 reveals that the ratio between the threshold parameters required for these two false alarm rates remains constant as a function of decl. This independence of the ratio on decl. enables us to apply a single decl.-dependent correction to the threshold parameter, which remains constant for all false alarm rates.

There is a slight decrease in the $TS_{threshold}$ as the decl. moves away from $+30°$, as shown in Figure 4. Even though setting the same threshold for targets at different declinations would have a maximum impact of no more than 0.2 on the false alarm rate per year, we still made correction to the threshold at different declinations. We used a quadratic function to fit this relationship, and the best fitted is shown as the dashed line in Figure 4. The $TS_{threshold}$ for one event per target per year as a function of decl. is expressed as

$$TS_{threshold}(\text{decl.}) = -1.47 \times 10^{-4}(\text{decl.}-30.18)^2 + 24.40 \quad (7)$$

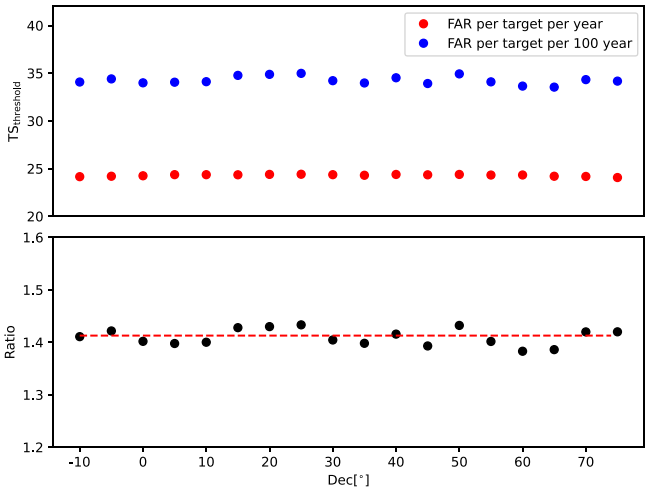

Figure 3. The threshold as a function of decl. The upper panel displays the $TS_{threshold}$ corresponding to the FAR of 1 event per target per year (red circles) and FAR of 1 event per target per century (blue circles). The lower panel illustrates the ratio of $TS_{threshold}$ for FAR of 1 event per target per century to that for FAR of 1 event per target per year, with the best fitted constant value of 1.412 (red dashed line).

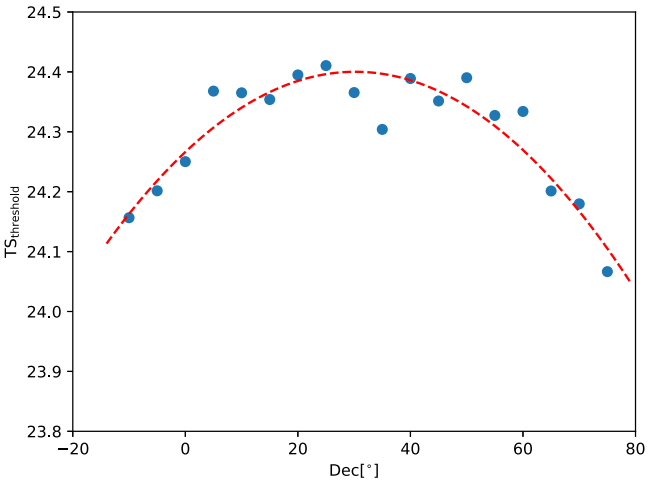

Figure 4. The function of $TS_{threshold}$ with respect to decl. for a false alarm rate of 1 event per year. The red dashed line represents the best fitted quadratic function.

According to the Equation (7), the decl.-dependent correction parameter is defined as:

$$C_{\text{decl.}} = \frac{TS_{threshold}(\text{decl.})}{TS_{threshold}(22)} = \frac{(\text{decl.}-30.18)^2}{(22-30.18)^2} \quad (8)$$

We applied this decl.-dependent correction $C_{\text{decl.}}$ to $TS_{threshold}$ of targets at different declinations, ensuring that the false alarm

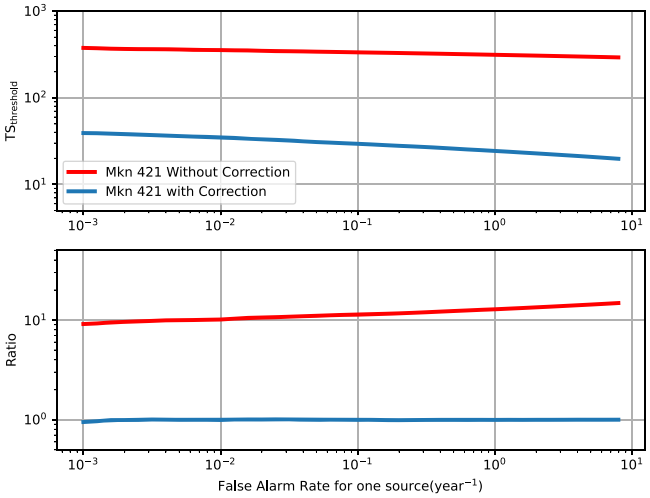

Figure 5. The TS threshold as in the upper panel shows the TS threshold for strong steady sources without and with correction; in the lower panel, they represent the ratio of the $TS_{threshold}$ with and without correction to the $TS_{threshold}$ of background regions.

rates at different declinations are consistent with the target at Crab position.

3.4.3. False Alarm Rate with Strong Emission

Strong targets with steady emission tend to generate higher TS values compared to targets without steady emission. Setting the same $TS_{threshold}$ as that of the background regions would lead to an underestimation of the false alarm rate. Therefore, we need to consider this effect to ensure that the false alarm rate for strong emission sources matches that of the background regions.

To address this, we utilize the simulation approach mentioned above. When considering the presence of steady emission sources, we account for the fluctuations caused by steady emission added to the background. Unlike before, where the count of the background window followed a Poisson distribution with a mean of $\alpha * N_{\rm off}$, when considering the presence of steady emission sources, an additional term is included in the mean of the Poisson distribution for the background window count. The mean count for the background window is set as $\alpha N_{\rm off} + R_{\rm tar} * \alpha N_{\rm off}$, where $R_{\rm tar}$ represents the relative excess of the target source observed by the WCDA with respect to the background window. $R_{\rm tar} = ({\rm ON_{all}} - \alpha * {\rm OFF_{all}})/(\alpha * {\rm OFF_{all}})$, where $\rm ON_{all}$ and $\rm OFF_{all}$ are the total on-source and off-source counts collected from the vicinity of the strong target over the entire data set. In this study, for Mkn 401, the values of $R_{\rm tar}$ are 0.11, 0.54, 1.79, 3.40, 5.89, 1.31 for bin 0 to bin 5 respectively, while for Mkn 501, the values are 0.03, 0.16, 0.64, 1.49, 3.44, 1.23.

In Figure 5, the upper panel illustrates the threshold for Mkn 421 with and without correction. The lower panel demonstrates

Table 3
The Threshold Parameter $TS_{threshold}$, Defined in Equation (6), Controls the False Alarm Rate of the Flare Detection Algorithm

Category	Number	$TS_{Threshold}$
I: Mkn 421, Mkn501	2	23.28
II: TeVCat extragalactic sources	64	30.94
III: Nearby 3FHL extragalactic sources ($z < 0.3$)	82	31.46
Total	148	···

that with the correction, we are able to effectively align the false alarm rate in the presence of steady sources with that of the background regions as shown in Figure 2.

The 148 selected target sources are classified into three categories based on the observation: (I) two well-known sources detected by LHAASO-WCDA, Mkn 421 and Mkn 501, (II) extragalactic sources from TeVCat, and (III) nearby extragalactic sources from 3FHL. In the current monitoring scheme, the expected false alarm rate for all selected target sources has been set to 10 occurrences per year with equal weight for these three categories. The specific TS threshold values chosen for the first category are 23.28, for the second category are 30.94, and for the third category are 31.46, as listed in the third column of Table 3. Once a source were detected to exceed its threshold, an alarm email would be sent to the people within the working group. Besides occasional alarm email, a daily summary reports about all selected target sources of past day are automatically sent to the relative working group.

4. Sensitivity of the Flare Monitor

Next, we examine the sensitivity of the flare monitor to flares with different properties. The flux, duration and source decl. of the flare can all impact the probability of detection at which the flare is detected. Although there are many complex models to describe the light curves of flares, for the sake of simplicity, we only consider the sensitivity in the case of the constant flare form. We calculate the sensitivity by injecting flares with the same spectral index as the Crab detected by LHAASO. For the off-source window, we sample from a Poisson distribution with a mean of m_i, and for the on-source window, we sample from a distribution with a mean of $\alpha * m_i + f * U_{\rm Crab}$, where f is the flux of the flare in Crab Units($U_{\rm Crab}$).

At the decl. of the Crab Nebula, we performed simulations to study the relationship between sensitivity, duration, and flux, while maintaining a false alarm rate of 10 events per year for the entire category. Figure 6 shows the detection probability for the fiducial flare with varying flux as a function of duration. As expected, increasing either the flux or the duration improves the detection probability.

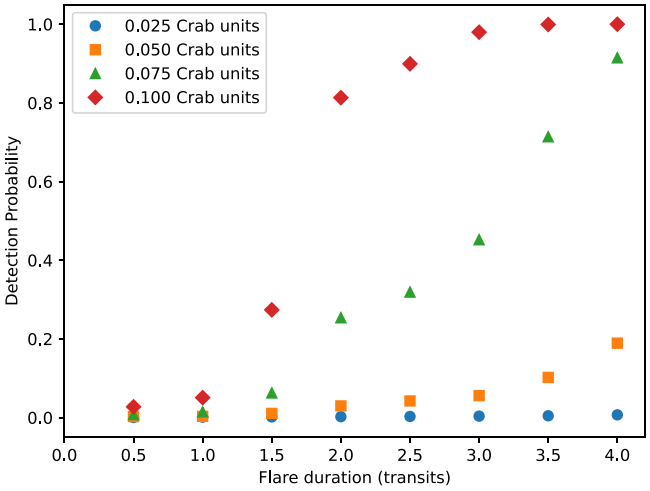

Figure 6. The detection probability as a function of flare duration. Different points represent the sensitivity for flares with fluxes equal to 0.025, 0.05, 0.075, 0.10 Crab Units.

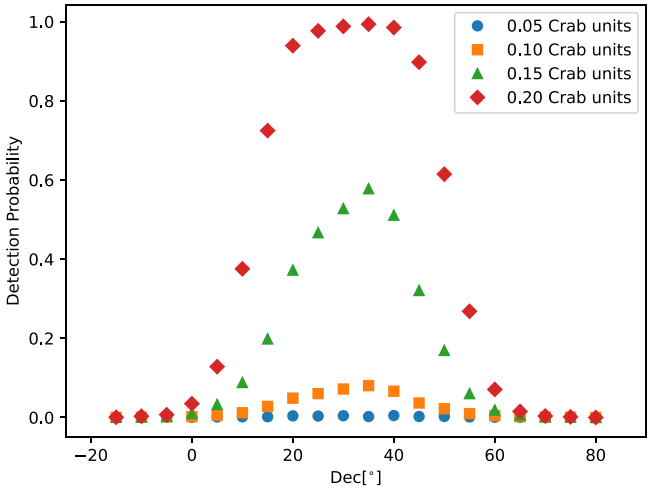

Figure 7. The detection probability as a function of decl. The sensitivity of monitoring system for flares lasting one day with 0.05, 0.10, 0.15, 0.20 Crab Units is considered.

Due to the reduced number of events at high zenith angles, the sensitivity of the monitor is strongly dependent on the decl. of the target source. Figure 7 depicts the sensitivity of the monitor to flare at different decl., based on 10 events false alarm rate for the target collection and with a flare duration of only 1 day. The data points in this figure take into account the decl.-dependent correction to the $TS_{threshold}$. It is evident that the sensitivity decreases significantly as the decl. moves away from $+30^{\circ}$ (the latitude of LHAASO).

5. Test Run with LHAASO-WCDA Data

During the test run, using the LHAASO-WCDA real-time alert system, on 2024 February 8 a TeV gamma-ray flare from 1ES 1959+650 was detected, WCDA observed an increase in the gamma-ray flux from the blazar starting at MJD = 60347.02, up to MJD = 60348.33 the accumulated pre-trial significance reached 8.7 standard deviations, with an integrated flux above 1 TeV exceeding 0.5 Crab Unit. An alert to ATel #16437 (Xiang et al. 2024b) is promptly issued, several multi-wavelength and multi-messenger follow-up observations were conducted by different detectors cross the world. The details are summarized in the following:

1. At the X-ray band, in ATel #16449 (Kapanadze 2024), Swift-XRT detector also discovered that 1ES 1959+650 was in a strong X-ray flare state, approximately 2.2 times higher than over-all observations using the X-ray Telescope with highly overlap time duration with LHAASO-WCDA observation.
2. At the GeV band, in ATel #16456 (Buson 2024) and GCN#35746, preliminary analysis from Fermi-LAT observations between MJD 60338 and 60357 (2024 January 29–February 17) indicates that the blazar has been in a high state for a month, with a monthly average flux ($E > 100$ MeV) of flux $= (1.8 \pm 0.2)x10^{-7}$ ph cm^{-2} s^{-1}, and index $= 1.67 \pm 0.05$. This is approximately four times the average flux reported in the Fourth Fermi LAT Source Catalog.
3. At neutrino muti-messenger point of view, IceCube also conducted a search within a 36 days time window (from 2024 January 15 00:00:00 UTC to 2024 February 20 00:00:00 UTC) and did not detect any signals, providing an upper limit on the time-integrated muon-neutrino flux from the source. Specifically, $E^2dN/dE = 1.1 \times 10^{-1}$GeV cm^{-2} at 90% CL (Thwaites et al. 2024).

On 2024 March 8, another Atel#16513 (Xiang et al. 2024a) about radio galaxy IC 310 is issued, this alert also triggers positive follow-up observation from VERITAS experiment (Furniss 2024), the detailed information about the alert and follow-up observation could be found in Table 4.

In a short summary, these series of related muti-wavelength and multi-messenger observation have been demonstrated and established a very good example of the capabilities of the LHAASO-WCDA real time alert system.

6. Summary and Outlook

The LHAASO-WCDA real-time flare monitor has been fully operated since end of 2023, and started to share the alerts to MAGIC collaboration from 2024 January. Up to now several Atels have been announced, a series of related muti-wavelength and multi-messenger observations have been conducted across the world-wide-level.

Table 4
LHAASO-WCDA Real-time Monitor Alerts

Alert No.	ATel No.	Detector	Title
No.1(1ES 1959+650)	Atel#16437	LHAASO-WCDA	LHAASO detects TeV Gamma-ray Activity from 1ES 1959+650
	Atel#16449	Swift-XRT	Strong X-Ray Flare in the TeV-Detected Blazar 1ES 1959+650
	Atel#16456, GCN#35746	FERMI-LAT	Gamma-ray flaring activity from the blazar 1ES 1959+650 observed with the Fermi-LAT
	Atel#16462	IceCube	1ES 1959+650: Upper limits from a neutrino search with IceCube
No.2(IC 310)	Atel#16513	LHAASO-WCDA	LHAASO detects rapid variability in TeV Gamma-rays from the galaxy IC 310
	Atel#16535	VERITAS	VERITAS Detection of Elevated VHE Emission from IC 310
	Atel#16540	LHAASO-WCDA	LHAASO detection of renewed TeV activity from the radio galaxy IC 310

The LHAASO-WCDA real-time flare monitor aims to facilitate coordinated observations, offering an opportunity to unravel the mysteries surrounding blazars, their VHE emission, and their jet mechanisms. To be more specific, one of purposes is to provide unbiased observations of TeV blazars, allowing for an increased sample of VHE flares. This contributes to understanding the nature and location of the dissipation region where the flares are generated, as well as the particle populations and acceleration mechanisms involved in producing these flares.

The next step of this monitoring system mainly involves two aspects. First, we are exploring additional monitoring topics, such as Novae bursting, and conducting discussions on full-sky blind searching. Second, we are focusing on enhancing our processes to minimize processing time.

Acknowledgments

This work is supported in China by NSFC grant No. 12393853, the Department of Science and Technology of Sichuan Province, China with grant No. 24NSFSC0449, NSFC grant No. U2031205. The authors particular thank Professor H.B. Hu, Professor Z.G. Yao for helpful discussions and suggestions.

ORCID iDs

M. Zha https://orcid.org/0000-0002-6911-5119
J. N. Zhou https://orcid.org/0000-0003-0343-5571

References

Abdollahi, S., Ackermann, M., Ajello, M., et al. 2017, ApJ, 846, 34
Aharonian, F., An, Q., Axikegu, et al. 2021, ChPhC, 45, 085002
Ajello, M., Atwood, W. B., Axelsson, M., et al. 2021, ApJS, 256, 12
Ajello, M., Atwood, W. B., Baldini, L., et al. 2017, ApJS, 232, 18
Bartoli, B., Bernardini, P., Bi, X. J., et al. 2011, NIMPA, 659, 428
Biller, S. D., Breslin, A. C., Buckley, J., et al. 1999, PhRvL, 83, 2108
Buson, S. 2024, ATel, 16456, 1
Cao, Z., Aharonian, F., An, Q., et al. 2024, ApJS, 271, 25
Dwek, E., & Krennrich, F. 2013, APh, 43, 112
Fleysher, R., Fleysher, L., Nemethy, P., Mincer, A. I., & Haines, T. J. 2004, ApJ, 603, 355
Furniss, A. 2024, ATel, 16535, 1
Ghisellini, G., Celotti, A., Fossati, G., Maraschi, L., & Comastri, A. 1998, MNRAS, 301, 451
Górski, K. M., Hivon, E., Banday, A. J., et al. 2005, ApJ, 622, 759
Kapanadze, B. 2024, ATel, 16449, 1
Li, T. P., & Ma, Y. Q. 1983, ApJ, 272, 317
Neronov, A., & Semikoz, D. V. 2007, JETPL, 85, 473
Stecker, F. W., de Jager, O. C., & Salamon, M. H. 1992, ApJL, 390, L49
Thwaites, J., Blaufuss, E., Santander, M., & Vandenbroucke, J. 2024, ATel, 16462, 1
Wakely, S. P., & Horan, D. 2008, TeVCat: An online catalog for Very High Energy Gamma-Ray Astronomy in Proc. 30th Int. Cosmic Ray Conf. 3 (Mexico City, Mexico: ICRC), 1341
Wilks, S. S. 1938, The Annals of Mathematical Statistics, 9, 60
Xiang, G., Zha, M., Yao, Z., Zhou, J., & Xing, Y. 2024a, ATel, 16513, 1
Xiang, G., Zha, M., Yao, Z., Zhou, J., & Xing, Y. 2024b, ATel, 16437, 1